



Originally published as:

Klemann, V., Martinec, Z., Ivins, E. R. (2008): Glacial isostasy and plate motion. - Journal of Geodynamics, 46, 3-5, 95-103

DOI: 10.1016/j.jog.2008.04.005

Glacial isostasy and plate motion

by

Volker Klemann¹, Zdeněk Martinec^{1,2}
and Erik Ivins³

¹Dept. Earth System Modelling, GeoForschungsZentrum Potsdam,
Potsdam, Germany

²Charles University in Prague, Prague, Czech Republic

³Jet Propulsion Laboratory, California Institute of Technology,
Pasadena, USA

Abstract

The influence of glacial-isostatic adjustment (GIA) on the motion of tectonic plates is usually neglected. Employing a recently developed numerical approach, we examine the effect of glacial loading on the motion of the Earth's tectonic plates where we consider an elastic lithosphere of laterally variable strength and the plates loosely connected by low viscous zones. The aim of this paper is to elucidate the physical processes which control the GIA induced horizontal motion and to assess the impact of finite plate-boundary zones. We show that the present-day motion of tectonic plates induced by GIA is at, or above, the order of accuracy of the plate motions determined by very precise GPS observations. Therefore, its contribution should be considered when interpreting the mechanism controlling plate motion.

1 Introduction

Glacial isostatic adjustment (GIA) describes the ongoing readjustment of the Earth arising from the quasi-periodic mass redistribution between continental glaciers, ice sheets and the ocean during glacial cycles, of about 100 kyr in periodicity (Petit *et al.*, 1999). The fluctuation in global ice coverage during the last glaciation, extending over wide areas of North America, northern Europe and Antarctica, involved changes in ice-thicknesses of up to 4 km (Denton & Hughes, 1981; Tarasov & Peltier, 2004), with sea level in many areas being over 100 m below the present level (Fleming *et al.*, 1998), causing large deformations that remain active and detectable by modern geodetic techniques (Lambert *et al.*, 2001; Pagiatakis & Salib, 2003). Therefore, the ongoing GIA is usually taken into account when interpreting, for example, present-day secular trends in the Earth's gravity field and rotation axis, and long-term variations in sea level. GIA-induced horizontal motion inferred by space geodetic techniques has primarily been used in studies dealing with formerly glaciated regions such as Scandinavia or North America (James & Morgan, 1990; Milne *et al.*, 2001; Sella *et al.*, 2007). However, the present-day accuracy of such techniques and improved modelling of GIA enables us to study the induced horizontal motion globally and to assess its effect on the motion of all of the Earth's major tectonic plates.

The motion of the plates is predominantly driven by convective processes in the Earth's mantle with characteristic timescales of 1–100 Myr (Knopoff, 1964; Richter, 1973; McKenzie *et al.*, 1974).

There are two principal approaches for quantifying plate velocities: Geologically-based models like NUVEL-1A (DeMets *et al.*, 1994), that rely on the analysis of geomagnetic reversals and other geological and seismic data, represent plate velocities averaged over the last million years. In contrast, geodetically-based models like REVEL (Sella *et al.*, 2002) rely on the analysis of Global Positioning System (GPS) observations. The latter represent plate velocities averaged over the last decade and a half (A.D. 1993–2008). The GIA process, with a period of 0.1 Myr, therefore, represents an undetectable transient perturbation of the geologically-inferred model, but a detectable component in the geodetically-inferred secular trends used to construct the model. The usual way to eliminate the GIA-induced horizontal motion from GPS observations is to exclude those GPS observations that are recorded in areas near formerly glaciated regions (Sella *et al.*, 2002). The argument for such a procedure is that the GIA-induced horizontal displacements are about one order of magnitude smaller than the associated vertical displacements and are concentrated to the formerly glaciated regions (Peltier *et al.*, 1986; Lambert *et al.*, 2001). This approach does not, however, remove the effect of GIA from GPS observations completely, since GIA-induced horizontal motion is distributed over the entire globe with amplitudes of the order of one mm/yr (James & Morgan, 1990; Wang & Wu, 2006a). Since the plate velocities are of the order of a few cm/yr, the GIA-induced horizontal motion generally contributes less than 10 % of the total observed signal (Sella *et al.*, 2002). Despite such a small amplitude, this signal is present in the extremely precise continuous tracking

77 data of GPS (Calais *et al.*, 2006).

78 GIA induced horizontal motions are much more sensitive to
79 mechanical properties that lie above the mantle, and, as a
80 consequence, to lateral variations in lithosphere strength, than
81 are the GIA-induced vertical motions. Due to computational
82 rigor inherent to the modelling of viscoelastic lateral hetero-
83 geneities, various approximations, such as introducing some sym-
84 metries like a 2-D structure for a half-space model (Sabadini *et al.*,
85 1986; Kaufmann *et al.*, 1997) or axial symmetry for a spheri-
86 cal earth model (e.g. Wu & van der Wal, 2003; Martinec & Wolf,
87 2005; Klemann *et al.*, 2007) have been employed in past work.
88 Half-space models that consider structural features in 3-D are
89 constrained to regional GIA due to the neglect of spheric-
90 ity: Europe (Marotta & Sabadini, 2004; Kaufmann & Wu, 1998,
91 2002; Steffen *et al.*, 2006) Laurentia (Wu, 2005) and Antarctica
92 (Kaufmann *et al.*, 2005).

93 More recently, global approaches use spherical finite element
94 models with a grid strategy that incorporates lateral variations in
95 mantle viscosity and lithospheric strengths (Wang & Wu, 2006a,b)
96 or plate boundaries (Latychev *et al.*, 2005; Whitehouse *et al.*, 2006).
97 Predictions from such models form a more realistic basis for com-
98 parison to the observed global horizontal motions. In this study,
99 we specifically demonstrate the importance of plate boundaries on
100 the GIA-induced horizontal motion and, therefore, better decipher
101 how GIA places an imprint on observed plate-tectonic motion.

2 Modelling of GIA-induced motion

To examine how the GIA process effects plate motion, we approximate the Earth by a self-gravitating sphere with a linear viscoelastic rheology. The upper and lower mantles have uniform viscosities of 5×10^{20} Pa s and 10^{22} Pa s, respectively; the model accommodates a fluid core. The elastic part of viscoelastic rheology is considered incompressible with the elastic shear modulus and mass-density defined by the Preliminary Reference Earth Model. The spectral finite element method developed by Martinec (2000) is applied which allows strong lateral viscosity contrasts to be considered, including lateral variations in lithosphere thickness. The resolution in horizontal directions is represented by spherical harmonics up to degree 170 which corresponds to a spatial resolution of about 120 km, and vertically by finite elements of 5 km in the lithosphere and upper mantle.

We define the base of the elastic lithosphere to be at the depth of the 1100 °C isotherm (Figure 1), assuming to be the characteristic temperature below which the Earth's material is dominated by elasticity for strains having time scales shorter than 0.1 Myr. The thickness of continental lithosphere is directly derived from a global thermal model, where we used the temperature profiles on a $5^\circ \times 5^\circ$ grid provided by Artemieva (2006). The thermal structure of the oceanic lithosphere is derived from its age (Müller *et al.*, 1997) by applying a simple plate-cooling model. The 1100 °C isotherm is calculated by assuming heat conduction inside the oceanic plate between the mantle of 1300 °C and surface of 0 °C (e.g. Turcotte & Schubert,

2002, p. 161). In order to consider the role of plate boundaries in the decoupling of shear stresses between the plates, the main plate boundaries taken from Bird (2003) are approximated as 200-km narrow zones of viscoelastic material, and further approximated assuming the same viscosity as the upper mantle (Figure 1).

The surface loading applied considers the main areas of glaciation (Laurentide, Greenland, Fennoscandia and Antarctica) over the last glacial cycle. The spatio-temporal evolution of the Laurentide and Greenland ice sheets are described by the standard ICE3G model (Tushingham & Peltier, 1991) for Laurentia, the Fennoscandian ice sheet by the SCAN model (Lambeck *et al.*, 1998), and the Antarctic ice sheet by the ICE3G model. This model gives a global sea-level fall of -105 m at the Last Glacial Maximum (LGM) (Hagedoorn *et al.*, 2006). The mass conservation principle is applied for water exchange between ocean and ice sheets during the Pleistocene glaciation where, for simplicity, we uniformly reduced the sea-level in accord with continental ice volume change assuming fixed coast lines.

3 Influence of tectonic plates on GIA-induced motion

The spatio-temporal changes in surface-mass load during the Pleistocene glaciation induce vertical mantle-material flow resulting in present-day surface-uplift rates of up to 20 mm/yr. This material flow is accompanied by horizontal material transport inside the

mantle (James & Morgan, 1990). Since the viscosity of the upper mantle is significantly lower than that of the lower mantle, the horizontal flow is concentrated in the layer between a highly viscous lower mantle (below 670 km depth) and the elastic lithosphere.

Figure 2 shows the horizontal and vertical present-day velocities induced by the assumed late-Pleistocene glaciation cycle. The present-day GIA-induced horizontal flow displays a hemispheric pattern and, generally, the geometry of this flow means that it orients toward the areas of present-day uplift. The flow of the northern hemisphere is induced by the formerly glaciated regions of Fennoscandia, Greenland and Laurentia and is directed northward, while the flow of the southern hemisphere, induced by the glaciation of Antarctica is directed southward (e.g. Wang & Wu, 2006a). Furthermore, abrupt changes in the horizontal velocities appear at several plate boundaries, for example at the boundary between the Pacific and North American plates, the Indian and Antarctic plates and between the Australian and Antarctic plates (Figure 2, right). These features do not appear if a model with a uniform lithosphere thickness of 100 km is assumed (Figure 2, left).

More striking is to consider the spatial gradient of the displacement rate, $\nabla \dot{\mathbf{u}}$. Regarding the strain rate, $\dot{\epsilon}$, we show in Figure 3 the divergence of the surface components and its second invariant:

$$\text{div}_h \dot{\mathbf{u}} = \dot{\epsilon}_{\theta\theta} + \dot{\epsilon}_{\phi\phi} , \quad (1)$$

$$\dot{\epsilon}_{\text{h,II}} = \sqrt{\dot{\epsilon}_{\theta\theta}^2 + \dot{\epsilon}_{\phi\phi}^2 + 2 \dot{\epsilon}_{\theta\phi}^2} . \quad (2)$$

Regarding the vorticity, $\boldsymbol{\omega}$, it is important to monitor its radial

component and its absolute value:

$$\omega_r = \mathbf{e}_r \cdot (\nabla \times \dot{\mathbf{u}}), \quad (3)$$

$$\omega = |\nabla \times \dot{\mathbf{u}}|. \quad (4)$$

171 Apart from the last quantity, wherein radial gradients are also in-
172 volved, the quantities (Eqs. 1–3) are defined by the surface com-
173 ponents of the displacement field. First, it should be mentioned
174 that positive divergence means dilation, whereas negative diver-
175 gence means compression of the surface plane. For the radial vor-
176 ticity, a negative sign indicates a dextral rotation of an idealized
177 surface element whereas a positive sign indicates a sinistral rotation.
178 The other two components are positive by definition. The diver-
179 gence shows the known features of dilation of the formerly glaciated
180 regions which are surrounded by areas of compression as direct con-
181 sequence of the uplift pattern. In addition, the plate boundaries
182 around Antarctica mainly show dilation whereas the Mid-Atlantic
183 ridge and the Arctic Lomonosov ridge show compression.

184 The second invariant of the surface strain rate shows a sim-
185 ilar pattern like the divergence, only the plate boundaries are
186 more pronounced in this plot. In comparison to the values in-
187 ferred for plate tectonic motion exceeding thousands of 10^{-9} /yr
188 Kreemer *et al.* (2003), the GIA contribution represents a small per-
189 turbation. The radial vorticity directly resembles the toroidal mo-
190 tion, which does not appear for a 1-D earth model. Such a model
191 if loaded by a surface pressure will only experience spheroidal mo-
192 tions and, therefore, the radial vorticity is zero. Here, the largest
193 amplitudes appear at the plate boundaries while vorticity in the

regions of large uplift are negligible. The total vorticity is almost a factor of 10 larger than the radial component alone, as it collects information pertaining to all components of the deformation-rate tensor including the tilting of the surface, which tends to follow the migrating peripheral bulge (James & Bent, 1994). Therefore, the largest amplitudes surround the former glacial maxima, where the strongest uplift gradients appear (compare Figure 2). This feature is generally common to all GIA models, appearing in the 1-D earth model as well. The plate boundaries showing gradients in horizontal motion are diminished.

The degree variance spectra shown in Figure 4 provide insight into the partitioning of surface motion between the spheroidal and toroidal component (e.g. Forte & Peltier, 1987). Shown are the degree variances

$$\sigma_U^2(l) = \sum_{m=0}^l U_{lm} U_{lm}^* \quad (5)$$

$$\sigma_V^2(l) = \sum_{m=0}^l V_{lm} V_{lm}^* \quad (6)$$

$$\sigma_W^2(l) = \sum_{m=0}^l W_{lm} W_{lm}^* \quad (7)$$

of the vertical and horizontal spheroidal component, U_{lm} , V_{lm} , and the toroidal component, W_{lm} , of the velocity field at the surface as function of Legendre degree, l , and order m (see Eq. 8). Asterix, *, denotes the conjugate complex. Proportional to these quantities are the surface divergence and radial vorticity which are scaled by $l(l+1)/R$ with respect to V_{lm} and W_{lm} (e.g. Čadek & Ricard, 1992). The variances show that the toroidal motion reaches the amplitude of the spheroidal V component for $l \geq 5$. An equipartitioning of

kinetic energy also appears in the motion of the tectonic plates (e.g. Hager & O'Connell, 1978; Čadež & Ricard, 1992; Bercovici, 1995) where, due to the existence of lithospheric plates the efficiency of convection as a poloidal motion is enhanced by reducing the overall dissipation in the system (Bercovici, 2003). Here, the equipartitioning gains strength at degrees larger than 3, whereas for longer wavelengths the spheroidal motion dominates. An exposition on this topic is beyond the scope of this paper, but the controlling mechanics are likely to have strong analogies to the convective systems described by Bercovici (2003). The vertical motion, dotted lines, is dominated by buoyant forces that cause uplift in the previously glaciated areas and does not noticeably change if we consider lateral lithospheric variations. This is also shown in Figure 2 where no broad scale variations in the uplift process are predicted.

In order to better understand the dynamics appearing in these numerical solutions, the material flow pattern along a cross-section passing through the main areas of former/current glaciation in the northern hemisphere is shown in Figure 5. The lateral flow shown in the upper panels is mainly confined to the upper mantle and flow in the lower mantle is only visible below Laurentia, a feature which confirms the fact that the regional GIA is additionally affected by the lower mantle (Wolf *et al.*, 2006) whereas for Fennoscandia motion is, relatively, confined to upper mantle processes (Wieczerkowski *et al.*, 1999; Martinec & Wolf, 2005). The lateral mantle-material flow manifests a shear traction on the overlying plates. The traction, consequently, pulls the tectonic plates toward the former glaciation centres of Laurentia, Greenland and

Fennoscandia. The role of the mid-Atlantic ridge as a soft plate boundary is complex because ongoing GIA is occurring on both sides of the cross-section. Figure 6 more closely examines the upper mantle for the same profile. In the right panel of Figure 6 the flow pattern for a 1-D earth model is shown for comparison. Although the flow shown in the upper panels of Figure 6 are similar (which corresponds to the similar flow around the previously glaciated regions at the surface, see Figure 2), it is evident that the lateral flow pattern tracks the viscous portion of the upper mantle and is strikingly discontinuous at the lithospheric base. The discontinuity in the motion becomes more evident in the vorticity (Figure 6, lower panels), as the intensity of the parameter makes a step-like change across the rheological boundaries. So, the vector component normal to the plane (off-plane) describes the rotation of idealized rigid particles in the plane, sinistral in red and dextral in blue. The vertical component of the vector shown here describes the radial vorticity as in Figure 2 and the horizontal in-plane component exhibits a tilting of the particle out of the plane. For the 1-D earth model it is evident that within the earth radial vorticity is absent. Again, recall that this component is solely described by a toroidal field. The pattern of the horizontal components for the two models are similar in this portion of the spherical earth, especially in the lithosphere. The amplitude of vorticity is largest near the boundaries of the upper mantle, whereas they are almost constant inside the elastic lithosphere, a consequence of near-unidirectional motion in the lithosphere. Due to the direction of the profile normal to the load margins, the in-plane components of vorticity are quite small

in comparison to the normal component. Inside the lithosphere, the normal component of rotation resembles the tilting of the surface according to the uplift gradient with distance from the former centres of glaciation. The rotation is sinistral to the right and dextral to the left of the respective uplift centres. The horizontal in-plane component is one order of magnitude smaller than the off-plane component. The vertical component, ω_r , becomes evident in the upper mantle where the lithosphere base shows a significant slope, e.g. at 35° on the profile. Here, ω_r is also comparable to the horizontal in-plane components and the discontinuity in the off-plane component across the lithospheric base is also evident.

In order to resolve the effect of a low-viscosity plate boundary on the GIA-induced flow, we choose a second cross-section (Figure 7) that passes through the Southeast-Indian ridge between the Australian and Antarctic plates. For this cross section it is striking that the GIA-induced horizontal velocities are relatively subdued north of the Southeast-Indian ridge and abruptly promoted south of the ridge. In the vicinity of the ridge, the sub-surface horizontal velocities increase toward the surface, approximating the behaviour of material flow for the case of a free-slip boundary condition. The amplitude of the horizontal-velocity contrast is 2 mm/yr (Figure 8). Although this is only a small part of the observed 70 mm/yr spreading rate of this ridge, the presence of the ridge significantly changes the material flow pattern in comparison to the case without a plate boundary (Figure 8, bottom panel). Traversing across the Southeast-Indian ridge, the abrupt change in horizontal velocity is predicted in the 3-D earth model, while the change is much

smoother in the prediction of the corresponding laterally homogeneous model. The top panel shows that the uplift rate is relatively little influenced by the presence of the ridge.

4 Influence of GIA on plate motion

The motion of tectonic plates is usually represented by a rigid motion around a rotation pole. In order to compare the GIA-induced motion with the geodetically inferred plate motion in [Altamimi *et al.* \(2007\)](#), we calculate the incremental rotation of individual tectonic plates from the GIA induced horizontal velocities at the sites provided in their Table 7 applying a least squares fit (Appendix, Eq. 10). Table 1 shows the rotation poles and velocities given in [Altamimi *et al.* \(2007, Table 8\)](#) with those determined for the GIA-induced motion. For the chosen models, the largest rotation is exhibited in North America, as is shown in Figure 9. The vectors west of the North American continental divide show the considerable influence of the modeled plate boundaries (Figure 2). The latter facilitates an enhanced north-northwesterly and, consequently, a stronger rotation of the continent. This numerical experiment suggests that models of the geophysical forces that control North American plate motion might have to further consider GIA induced motions before advancing dynamical models that explain crustal motion at the 1–2 mm/yr level.

The model reference system is defined by fixing the center of mass and that no net rotation of the surface is allowed (Appendix, Eq. 9). In order to compare the GIA induced poles with those of

the observed plate motions, we subtract the respective GIA induced rotation vectors from the ITRF rotation vectors, $\Omega_{ITRF} - \Omega_{GIA}$ and consider the resulting changes in longitude, latitude and rotation velocity in the 4th to 7th column of Table 1. The rotational velocity of Antarctica and Europe are slightly reduced, whereas those of the Pacific and South American plate are unaffected by GIA. The other plates listed are enhanced by the effect of GIA. The shifts in the location of the rotation poles are at the level of about 1 degree. From the intercomparison of the perturbations considered here, we conclude that there is a ubiquitous influence of rheologically soft plate boundaries on plate rotations, intraplate horizontal velocities and on the generation of finite global toroidal deformation field. Each of these features may be detectable by modern space geodetic techniques.

5 Summary

This study shows that the GIA-induced horizontal velocities are globally of the order of 1 mm/yr, and are strongly influenced by lateral variations in lithosphere thickness and the presence of tectonic plate boundaries. The current level of accuracy in the detection of present-day horizontal motions approaches 1 mm/yr using space-geodetic techniques such as GPS. Therefore, GIA signals must be considered for modeling the mantle-wide dynamical causes of plate motion and of intraplate deformations. The present study essentially considers only one element of lateral variability, lithosphere thickness. Other viscosity variations in the upper mantle have to

be considered as shown by Wang & Wu (2006a) and Paulson *et al.* (2007). It should be noted that this study probes but one subset of the parameter space for predicting GIA-induced surface horizontal motion. Our results indicate the global importance of ongoing GIA in the interpretation of GPS time series for sites far away from the formerly glaciated areas, as these are non-negligible with respect to state-of-the-art kinematic and dynamic models of plate motion. The global consequences of GIA are amplified by the existence of soft plate boundaries. Further amplification could occur in model predictions that incorporate lateral variations of lithosphere thickness and variability in the mantle viscosity.

Acknowledgments

The work of the first author was supported by the priority program SPP 1257 of the German Research Foundation (DFG). The second author acknowledges the support from the Grant Agency of the Czech Republic through grant No. 205/06/0580. Suggestions of Roberto Sabadini and a further anonymous reviewer of a previous version of the paper are acknowledged as the suggestions to the current review process.

References

- Altamimi, Z., Collilieux, X., Garayt, B. & Boucher, C., 2007. ITRF2005: A new release of the International Terrestrial Reference Frame based on time series of station positions and Earth Orientation Parameters. *J. Geophys. Res.*, 112: B09401, doi:10.1029/2007JB004949. [13](#), [28](#)
- Artemieva, I. M., 2006. Global $1^\circ \times 1^\circ$ thermal model tc1 for the continental lithosphere: Implications for lithosphere secular evolution. *Tectonophysics*, 416: 245–277. [5](#), [26](#)
- Bercovici, D., 1995. On the purpose of toroidal motion in a convecting mantle. *Geophys. Res. Lett.*, 22: 3107–3110. [10](#)
- Bercovici, D., 2003. The generation of plate tectonics from mantle convection. *Earth Planet. Sci. Lett.*, 205: 107–121. [10](#)
- Bird, P., 2003. An updated digital model of plate boundaries. *Geochem. Geophys. Geosyst.*, 4: doi:10.1029/2001GC000252. [6](#)
- Čadež, O. & Ricard, Y., 1992. Toroidal poloidal energy partitioning and global lithospheric rotation during Cenozoic time. *Earth Planet. Sci. Lett.*, 109: 621–632. [9](#), [10](#)
- Calais, E., Han, J. Y., DeMets, C. & Nocquet, J. M., 2006. Deformation of the North American plate interior from a decade of continuous GPS measurements. *J. Geophys. Res.*, 111: B06402. doi:10.1029/2005JB004253. [4](#)
- DeMets, C., Gordon, R. G., Argus, D. F. & Stein, S., 1994. Effect of recent revisions to the geomagnetic reversal timescale on esti-

mates of current plate motions. *Geophys. Res. Lett.*, 21: 2191–
2194. [3](#)

Denton, G.H. & Hughes, T.J., 1981. *The Last great Ice Sheets*.
John Wiley, New York. [2](#)

Fleming, K., Johnston, P., Zwartz, D., Yokohama, Y., Lambeck, K.
& Chappell, J., 1998. Refining the eustatic sea-level curve since
the Last Glacial Maximum using far- and intermediate-field sites.
Earth Planet. Sci. Lett., 163: 327–342. [2](#)

Forte, A.M. & Peltier, W.R., 1987. Plate tectonics and aspherical
earth structure: the importance of poloidal–toroidal coupling.
J. Geophys. Res., 92: 3645–3679. [9](#)

Hagedoorn, J.M., Wolf, D. & Martinec, Z., 2006. An estimate of
global sea level rise inferred from tide gauge measurements us-
ing glacial isostatic models consistent with the relative sea level
record. *Pure Appl. Geophys.*, 164: 791–818. [6](#)

Hager, B.H. & O’Connell, R.J., 1978. Subduction zone dips and
flow driven by the plates. *Tectonophysics*, 50: 111–134. [10](#)

James, T.S. & Bent, A.L., 1994. A comparison of eastern North
American seismic strain-rates to glacial rebound strain-rates.
Geophys. Res. Lett., 21: 2127–2130. [9](#)

James, T.S. & Morgan, W.J., 1990. Horizontal motions due to
post-glacial rebound. *Geophys. Res. Lett.*, 17: 957–960. [2](#), [3](#), [7](#)

Kaufmann, G. & Wu, P., 1998. Lateral asthenospheric viscosity

variations and postglacial rebound: a case study for the Barents

Sea. *Geophys. Res. Lett.*, 25: 1963–1966. [4](#)

Kaufmann, G. & Wu, P., 2002. Glacial isostatic adjustment in

Fennoscandia with a three-dimensional viscosity structure as an

inverse problem. *Earth Planet. Sci. Lett.*, 197: 1–10. [4](#)

Kaufmann, G., Wu, P. & Wolf, D., 1997. Some effects of lateral

heterogeneities in the upper mantle on postglacial land uplift

close to continental margins. *Geophys. J. Int.*, 128: 175–187. [4](#)

Kaufmann, G., Wu, P. & Ivins, E.R., 2005. Lateral viscosity vari-

ations beneath Antarctica and their implications on regional re-

bound motions and seismotectonics. *J. Geodyn.*, 39: 165–181.

[4](#)

Klemann, V., Ivins, E., Martinec, Z. & Wolf, D., 2007. Models

of active glacial isostasy roofing warm subduction: Case of the

South Patagonian Ice Field. *J. Geophys. Res.*, 112: B09405,

doi:10.1029/2006JB004818. [4](#)

Knopoff, L., 1964. The convection current hypothesis. *Rev. Geo-*

phys., 2: 89–122. [2](#)

Kreemer, C., Holt, W.E. & Haines, A.J., 2003. An integrated

global model of present-day plate motions and plate boundary

deformation. *Geophys. J. Int.*, 154: 8–34. [8](#)

Lambeck, K., Smither, C. & Johnston, P., 1998. Sea-level change,

glacial rebound and mantle viscosity for northern Europe. *Geo-*

phys. J. Int., 134: 102–144. [6](#)

Lambert, A., Courtier, N., Sagawa, G. S., Klopping, F., Winester,
D., James, T. M. & Liard, J. O., 2001. New constraints on Lau-
rentide postglacial rebound from absolute gravity measurements.
Geophys. Res. Lett., 28: 2109–2112. [2](#), [3](#)

Latychev, K., Mitrovica, J. X., Tamisiea, M. E., Tromp, J. &
Moucha, R., 2005. Influence of lithospheric thickness variations
on 3-D crustal velocities due to glacial isostatic adjustment. *Geo-
phys. Res. Lett.*, 32: L01304, doi:10.1029/2004GL021454. [4](#)

Marotta, A. M. & Sabadini, R., 2004. The signatures of tectonics
and glacial isostatic adjustment revealed by the strain rate in
Europe. *Geophys. J. Int.*, 157: 865–870. [4](#)

Martinec, Z., 2000. Spectral–finite element approach for three-
dimensional viscoelastic relaxation in a spherical earth. *Geophys.
J. Int.*, 142: 117–141. [5](#), [23](#)

Martinec, Z. & Wolf, D., 2005. Inverting the Fennoscandian
relaxation-time spectrum in terms of an axisymmetric viscosity
distribution with a lithospheric root. *J. Geodyn.*, 39: 143–163. [4](#),
[10](#)

Mckenzie, D. P., Roberts, J. M. & Weiss, N. O., 1974. Convection
in the earth’s mantle: towards a numerical simulation. *J. Fluid
Mech.*, 62: 465–538. [2](#)

Milne, G. A., Davis, J. L., Mitrovica, J. X., Scherneck, H., Johann-
son, J. M., Vermeer, M. & Koivula, H., 2001. Space–geodetic
constraints on glacial isostatic adjustment in Fennoschandia. *Sci-
ence*, 291: 2381–2384. [2](#)

Müller, R. D., Roest, W. R., Royer, J.-Y., Gahagan, L. M. &
Sclater, J. G., 1997. Digital isochrons of the world's ocean floor.
J. Geophys. Res., 102: 3211–3214. [5](#), [26](#)

Pagiatakis, S. D. & Salib, P., 2003. Historical relative gravity obser-
vations and the time rate of change of gravity due to postglacial
rebound and other tectonic movements in Canada. *J. Geophys.*
Res., 108: 2406, doi:10.1029/2001JB001676. [2](#)

Paulson, A., Zhong, S. & Wahr, J., 2007. Limitations on the inver-
sion for mantle viscosity from postglacial rebound. *Geophys. J.*
Int., 168: 1195–1209. [15](#)

Peltier, W. R., Drummond, R. A. & Tushingham, A. M., 1986. Post-
glacial rebound and transient lower mantle rheology. *Geophys.*
J. R. Astr. Soc., 87: 79–116. [3](#)

Petit, J. R., Jouzel, J., Raynaud, D., Barkov, N. I., Barnola, J. M.,
Basile, I., Bender, M., Chappellaz, J., Davis, M., Delaygue, G.,
Delmotte, M., Kotlyakov, V. M., Legrand, M., Lipenkov, V. Y.,
Lorius, C., Pepin, L., Ritz, C., Saltzmann, E. & Stievenard, M.,
1999. Climate and atmospheric history of the past 420,000 years
from the Vostok ice core, Antarctica. *Nature*, 399: 429–436. [2](#)

Richter, F. M., 1973. Dynamic models for sea-floor spreading. *Rev.*
Geophys. Space Phys., 11: 223–287. [2](#)

Sabadini, R., Yuen, D. A. & Portney, M., 1986. The effects of upper-
mantle lateral heterogeneities on postglacial rebound. *Geophys.*
Res. Lett., 13: 337. [4](#)

482 Sella, G., Stein, S., Dixon, T.H., Craymer, M., James, T.S., Maz-
483 zotti, S. & Dokka, R.K., 2007. Observation of glacial isostatic
484 adjustment in “stable” North America with GPS. *Geophys. Res.*
485 *Lett.*, 34: L02306, doi:10.1029/2006GL027081. [2](#)

486 Sella, G.F., Dixon, T.H. & Mao, A., 2002. REVEL: A model for
487 recent plate velocities from space geodesy. *J. Geophys. Res.*, 107:
488 2081, doi:10.1029/2000JB000033. [3](#)

489 Steffen, H., Kaufmann, G. & Wu, P., 2006. Three-dimensional
490 finite-element modeling of the glacial isostatic adjustment in
491 Fennoscandia. *Geophys. J. Int.*, 250: 358–375. [4](#)

492 Tarasov, L. & Peltier, W.R., 2004. A geophysically constrained
493 large ensemble analysis of the deglacial history of the North
494 American ice-sheet complex. *Quat. Sci. Rev.*, 23: 359–388. [2](#)

495 Turcotte, D.L. & Schubert, G., 2002. *Geodynamics*, 2nd edn. Cam-
496 bridge University Press, Cambridge. [5](#)

497 Tushingham, A.M. & Peltier, W.R., 1991. Ice-3G: a new global
498 model of the late Pleistocene deglaciation based upon geophysical
499 predictions of post-glacial relative sea level change. *J. Geophys.*
500 *Res.*, 96: 4497–4523. [6](#)

501 Varshalovich, D.A., Moskalev, A.N. & Khersonskii, V.K., 1988.
502 *Quantum Theory of Angular Momentum*. World Scientific Pub-
503 lishing, Singapore. [23](#)

504 Wang, H. & Wu, P., 2006a. Effects of lateral variations in litho-
505 spheric thickness and mantle viscosity on glacially induced sur-

face motion on a spherical, self-gravitating Maxwell Earth. *Earth Planet. Sci. Lett.*, 244: 576–589. [3](#), [4](#), [7](#), [15](#)

Wang, H. & Wu, P., 2006b. Effects of lateral variations in lithospheric thickness and mantle viscosity on glacially induced relative sea levels and long wavelength gravity field in a spherical, self-gravitating Maxwell Earth. *Earth Planet. Sci. Lett.*, 249: 368–383. [4](#)

Whitehouse, P., Latychev, K., Milne, G.A., Mitrovica, J.X. & Kendall, R., 2006. Impact of 3-D Earth structure on Fennoscandian glacial isostatic adjustment: Implications for space-geodetic estimates of present-day crustal deformations. *Geophys. Res. Lett.*, 33: L13502, doi:10.1029/2006GL026568. [4](#)

Wieczerkowski, K., Mitrovica, J.X. & Wolf, D., 1999. A revised relaxation-time spectrum for Fennoscandia. *Geophys. J. Int.*, 139: 69–86. [10](#)

Wolf, D., Klemann, V., Wunsch, J. & Zhang, F.-p., 2006. A reanalysis and reinterpretation of geodetic and geomorphologic evidence of glacial-isostatic uplift in the Churchill region, Hudson Bay. *Surv. Geophys.*, 27: 19–61. [10](#)

Wu, P., 2005. Effects of lateral variations in lithospheric thickness and mantle viscosity on glacially induced surface motion in Laurentia. *Earth Planet. Sci. Lett.*, 235: 549–563. [4](#)

Wu, P. & van der Wal, W., 2003. Postglacial sealevels on a spherical, self-gravitating viscoelastic earth: effects of lateral viscosity

variations in the upper mantle on the inference of viscosity con-
trasts in the lower mantle. *Earth Planet. Sci. Lett.*, 211: 57–68.

4

A Appendix

The spectral representation of the displacement field follows the no-
tations in Martinec (2000), and splits the motion into a spheroidal
part represented by U_{jm} and V_{jm} and a toroidal part W_{jm} :

$$\mathbf{u}(r, \Omega) = \sum_{j=0}^{j_{\max}} \sum_{m=0}^j [U_{jm}(r) \mathbf{e}_r Y_{jm}(\Omega) + V_{jm}(r) \nabla_{\Omega} Y_{jm}(\Omega) + W_{jm}(r) \mathbf{L}_{\Omega} Y_{jm}(\Omega)] \quad (8)$$

where r is the radial distance and $\Omega = (\theta, \phi)$ are the colatitude
and longitude. The summations extend in Legendre degrees, j ,
from 0 to the maximum degree, j_{\max} , considered and in order m
from 0 to j . $Y_{jm}(\Omega)$ are the normalized scalar spherical harmonics
(e.g Varshalovich *et al.*, 1988). ∇_{Ω} denotes the angular part of the
gradient operator and $\mathbf{L}_{\Omega} = \mathbf{e}_r \times \nabla_{\Omega}$ stands for the angular part
of the angular momentum operator.

The conditions of center of mass invariance and no net rotation
are considered by assuming that for each epoch

$$\begin{aligned} \int_{V_0} \mathbf{u} \rho dV &= 0 \\ \int_{\Omega_0} \mathbf{u} \times \mathbf{e}_r d\Omega &= 0 \end{aligned} \quad (9)$$

holds, where V_0 is the earth's volume, Ω_0 is the earth's surface,
 ρ is the material density, \mathbf{e}_r is the radial unit vector and $d\Omega =$

546 $\sin \theta \, d\theta \, d\phi$.

In order to determine the rigid-plate rotation, we solve

$$\frac{1}{R} \begin{pmatrix} u_\theta(\theta_i, \phi_i) \\ u_\phi(\theta_i, \phi_i) \end{pmatrix} = \begin{pmatrix} -\sin \phi_i & \cos \phi_i & 0 \\ -\cos \theta_i \cos \phi_i & -\cos \theta_i \sin \phi_i & \sin \theta_i \end{pmatrix} \begin{pmatrix} \omega_x \\ \omega_y \\ \omega_z \end{pmatrix} \quad (10)$$

where R is the earth's radius. The displacement, u_θ, u_ϕ , at colatitude θ_i and longitude ϕ_i is given in polar coordinates originating from an incremental rotation vector $\boldsymbol{\omega} = \omega_x \mathbf{e}_x + \omega_y \mathbf{e}_y + \omega_z \mathbf{e}_z$ in Cartesian coordinates. The orientation of the Cartesian system with respect to the polar coordinates, (r, θ, ϕ) , is $\mathbf{e}_x = (1, \pi/2, 0)$, $\mathbf{e}_y = (1, \pi/2, \pi/2)$ and $\mathbf{e}_z = (1, 0, 0)$. The rotation vector is determined from the given displacement rates of the respective plate by applying a least-squares fit. The rotation pole then follows:

$$\begin{aligned} \Omega &= \sqrt{\omega_x^2 + \omega_y^2 + \omega_z^2}, \\ \Theta &= \arccos \frac{\omega_z}{\Omega}, \\ \Phi &= \arctan \frac{\omega_y}{\omega_x}. \end{aligned} \quad (11)$$

547 Its geographical coordinates are $\Phi = \text{longitude}$ and $90^\circ - \Theta =$
548 latitude . Figure 9 shows as an example of Table 1 the predicted
549 contribution to the plate motion of North America inferred from
550 modelled velocities at the ITRF stations.

Plate	ITRF/GIA			error/corr.		
	Lon. (°E)	Lat. (°N)	vel. (°/Myr)	Lon. (°E)	Lat. (°N)	vel. (°/Myr)
Antarctica	-125.3	59.8	0.223	±1.7	±0.9	±0.007
	135.5	34.0	0.005	2.2	-0.6	-0.002
	150.3	28.8	0.008	3.6	-0.4	-0.004
Australia	37.4	32.4	0.628	±0.4	±0.3	±0.003
	-118.3	-3.9	0.009	0.4	-0.3	0.007
	-105.8	1.9	0.006	0.4	-0.2	0.004
Eurasia	-96.0	56.3	0.261	±1.0	±0.5	±0.003
	-52.4	-16.3	0.009	-2.4	1.4	-0.001
	-56.7	-13.0	0.006	-1.6	1.0	-0.001
N. America	-87.4	-4.3	0.192	±0.6	±0.9	±0.002
	153.7	3.5	0.004	1.1	-0.0	0.002
	136.5	-39.8	0.015	2.3	2.9	0.008
Pacific	112.9	-62.6	0.682	±0.7	±0.2	±0.004
	52.0	36.3	0.002	0.3	-0.1	0.001
	9.5	11.4	0.003	0.5	-0.0	0.001
S. America	-129.6	-16.8	0.121	±2.1	±1.6	±0.003
	-19.9	-18.4	0.008	-3.6	1.6	0.002
	-9.9	-27.0	0.006	-2.1	1.5	0.002

Table 1: Absolute rotation poles for different plates from ITRF2005 (1st line of respective plate), GIA-induced component for 1-D earth model (2nd line) and for 3-D earth model (3rd line). The 4th to 7th column presents the respective errors in the determination of the ITRF poles and below the corrections to the ITRF poles if they are reduced by the GIA induced components. The table is designed to show the influence of a plate structure, not to give a realistic prediction

Figure 1: Mosaic of elastic lithosphere thickness defined by the depth of the 1100 °C isotherm inferred from the thermal structure of continental lithosphere ([Artemieva, 2006](#)) and age structure of oceanic lithosphere ([Müller *et al.*, 1997](#)). Plate boundaries (purple lines) are approximated by 200 km wide zones with the same viscosity as the upper-mantle.

Figure 2: Prediction of present-day surface velocities induced by the last glacial cycle with a laterally homogeneous lithosphere structure (left) and the considered 3-D earth model (right). Purple areas denote the considered plate boundaries.

Figure 3: Spatial surface fields related to the deformation rate according to (1)–(4): divergence in surface plane, second invariant of surface strain rate, radial component of rotation rate and absolute value of rotation rate.

Figure 4: Degree variance spectra of spheroidal and toroidal surface motion (left) and the derived quantities of surface divergence and radial vorticity (right). The spheroidal velocities are splitted into its horizontal contribution (solid lines) and its radial contribution (dotted lines).

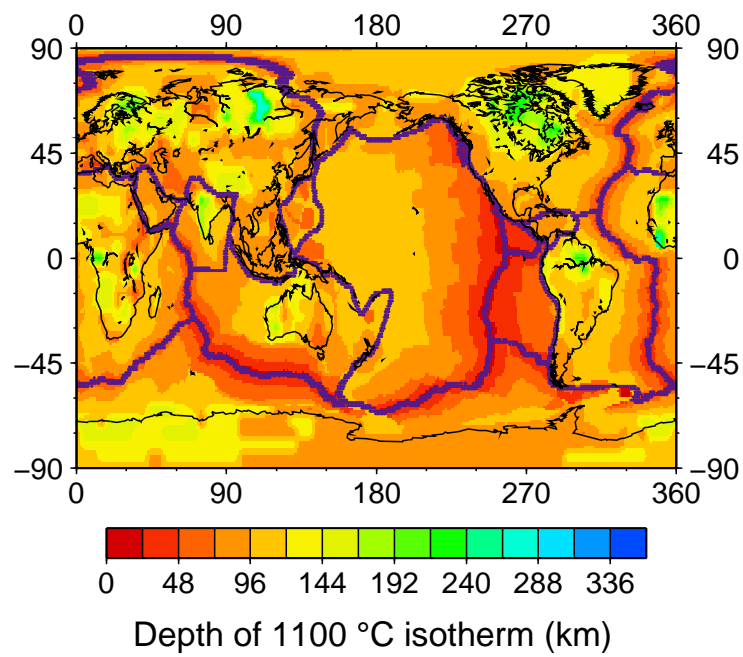
Figure 5: Present-day GIA-induced velocities along a cross-section passing through areas that contain the Laurentide (LIS), Greenland (GIS) and Fennoscandian (FIS) ice sheets, respectively. The upper panel shows the ice-sheet extent (blue line) and thickness at the last glacial maximum relative to present day. The profile of the cross section is marked in red. The plate boundaries are plotted in purple. The lower panel shows the present-day GIA-induced velocities in the plane of the cross section (vectors) and perpendicular to the plane (blue indicates a flow directed into the plane). The inverted triangle denotes the position of the mid-Atlantic ridge, dashed red lines denote the base of the effective elastic lithosphere and the boundary between upper and lower mantle.

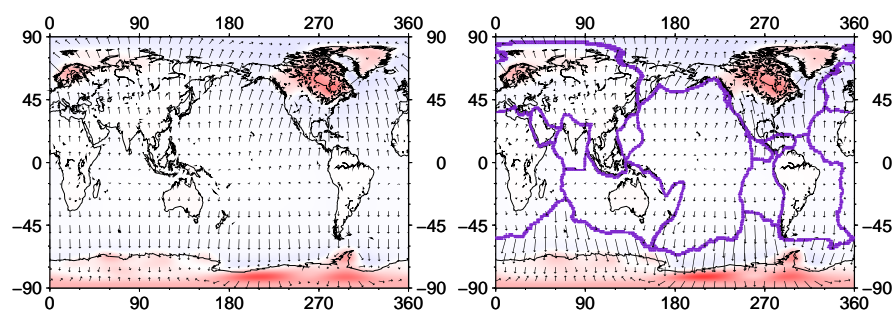
Figure 6: Present day velocity (upper panels) and vorticity (lower panels) on profile I over a limited mantle/lithosphere range. Fields for a 1-D earth model with 100 km lithosphere thickness are presented on the right. The red lines indicate the top and base of the viscoelastic upper mantle. At the top, the inverted triangle shows the position of the mid-Atlantic ridge and the rectangulars the extension of the glacial loads at LGM.

Figure 7: Present-day GIA-induced velocities along a cross-section beginning in Australia, passing through the Southeast-Indian ridge and ending in the Antarctic ice sheet (AIS). For details see Figure 5.

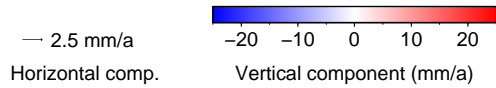
Figure 8: Horizontal and vertical present-day GIA-induced surface velocities along the cross-section shown in Figure 7. Velocities for the cases where lateral variations in lithosphere thickness and the presence of the Southeast-Indian ridge are considered are plotted with solid lines (3-D) and where they are not considered with dashed lines (1-D). Thick and thin lines in the bottom panel denote the horizontal motion in- and perpendicular to the plane of the cross section, respectively. The inverted triangle denotes the position of the Southeast-Indian ridge.

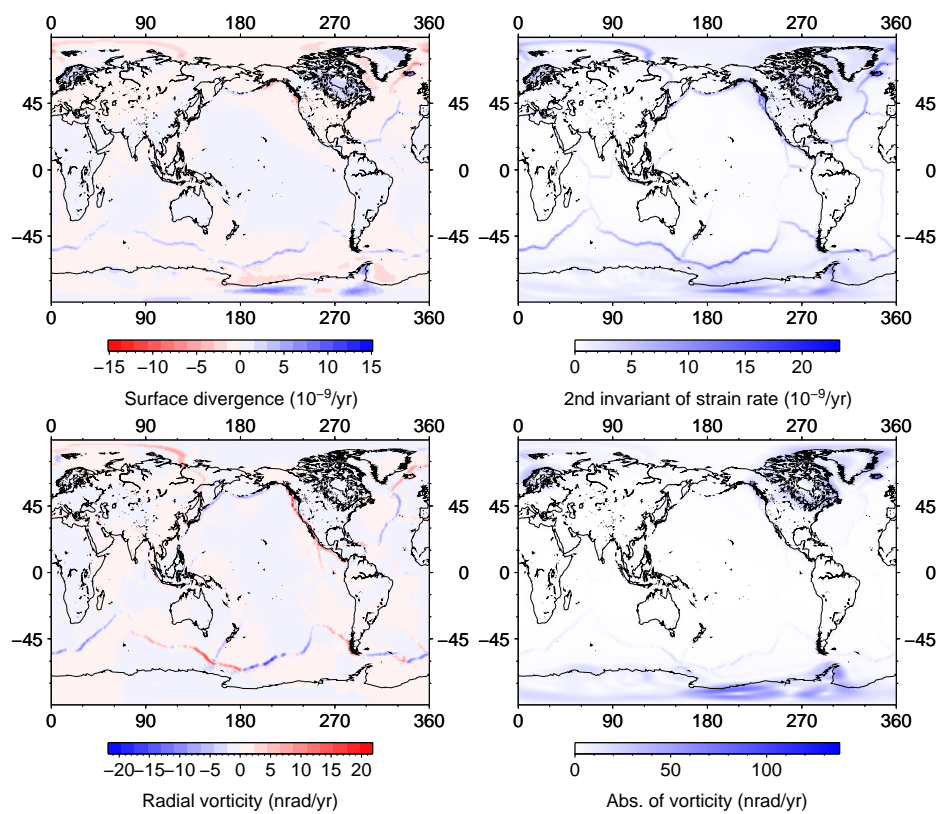
Figure 9: Horizontal present-day GIA-induced surface velocities for rigid plate sites of North America considered in the ITRF2005 (Altamimi *et al.*, 2007) for the 1-D earth model (left) and 3-D earth model (right) of the analysis presented in the paper. Black arrows denote the induced surface velocities and red arrows the velocities due to a rigid rotation with parameters given at the top of each plot.

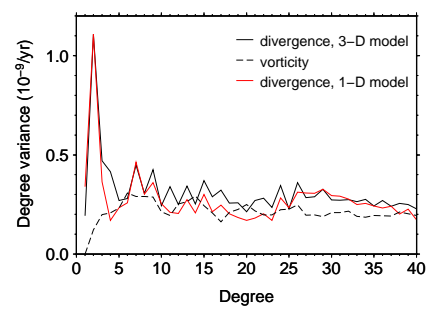
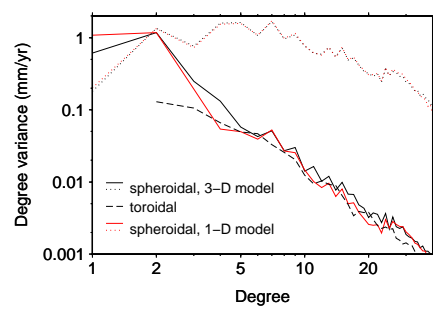


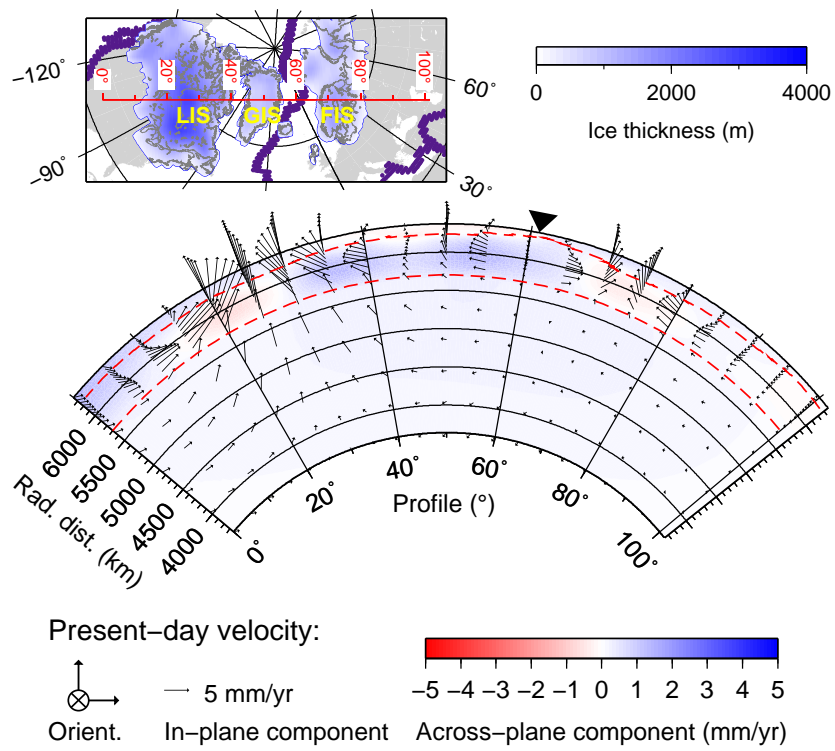


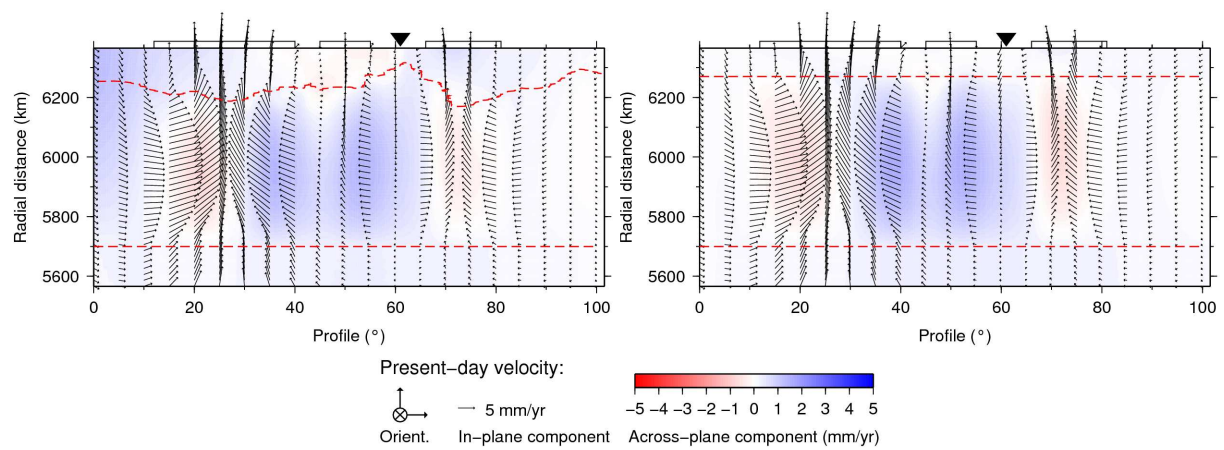
Present-day velocities:

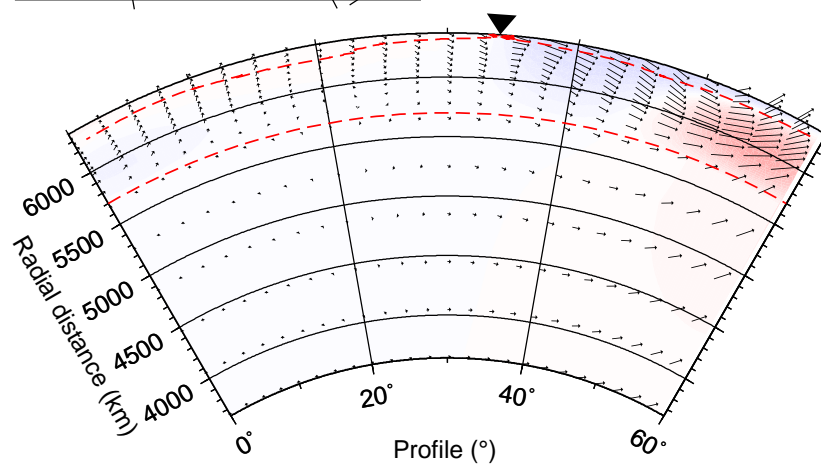
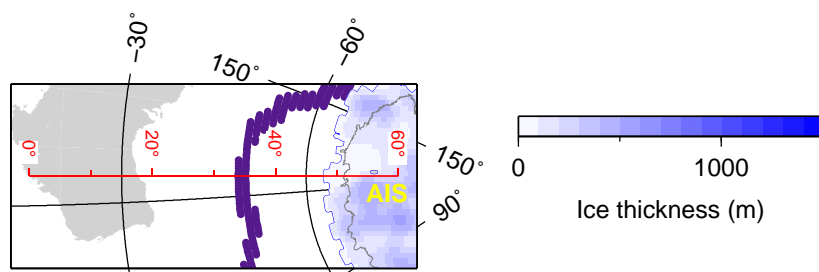




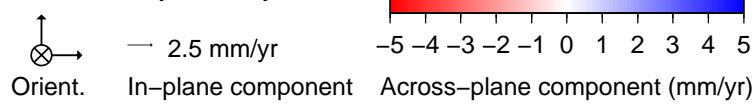


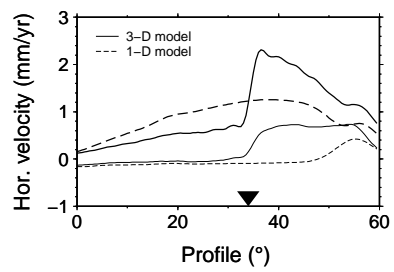
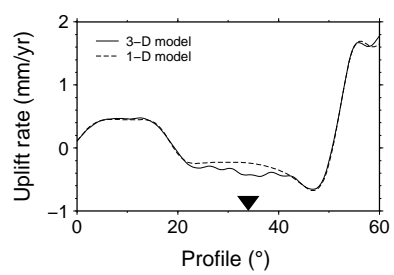




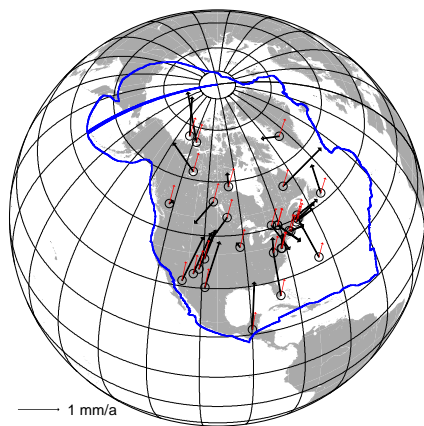


Present-day velocity:





(Lon=153.7 °E, Lat= 3.5 °N, $\Omega=4.2\text{e-}03$ °/Myr)



(Lon=136.5 °E, Lat=-39.8 °N, $\Omega=1.5\text{e-}02$ °/Myr)

